Numerical Solution of Two-dimensional Channel Flow of Viscous Incompressible Fluid past an Elliptic Cylinder

AUTHOR(S):

ANTOKU, Mitsuro; SAKURAI, Takeo; TAKEDA, Hidenori

Numerical Solution of Two-dimensional Channel Flow of Viscous Incompressible Fluid past an Elliptic Cylinder

by

Mitsuro ANTOKU, Takeo SAKURAI and Hidenori TAKEDA

(Received September 29, 1986)

Abstract

We studied a two-dimensional flow of viscous incompressible fluid past a thin elliptic cylinder in a rectilinear channel. The major axis of the cylinder has the same length as the channel width, and the center of the cylinder is placed on the midplane of the channel. Reynolds number R and the angle of attack θ of the cylinder range, respectively, between 50 and 1000 and between 0° and 40°.

The new upwind difference scheme by Kawamura Kuwahara (1984) is applied to the stream function-vorticity formalism of the Navier-Stokes equations. The boundary-fitted curvilinear coordinate systems by Thompson et al (1976) are used to transform the physical plane onto a simple calculation plane. The line-Jacobi method of iteration is applied to the solution of the Poisson type equation of the stream function. The Euler explicit method of solution is applied to the solution of the vorticity equation.

Our main results are as follows:

(1) We clarify the boundary between the steady and unsteady flows in an R-θ plane. We also study processes by which vortices are born near the cylinder, brought away into the "main" Poiseuille flow, and then decay by the effect of viscosity.

(2) We show, for cases of $\theta = 0°$, that our results on the drag coefficient C_D can be expressed well by Imai's (1958) drag formula : $C_D = A + B \cdot R^{-0.5}$ within our range of R, where A and B are arbitrary coefficients to be determined by our results for the two values of R.

(3) As a practical application, we compare our results with those of Kimura et al's (1980) experiments on a butterfly valve, and obtain qualitatively good agreement for the pressure drop due to the valve, and for the torque-coefficient. An interesting fact is that our results well reproduce a steep crest in the torque-coefficient diagram versus angle of attack, which is characteristic of experimental results.

Department of Aeronautical Engineering, Faculty of Engineering, Kyoto University, Kyoto, Japan

1. Introduction

The study of a channel flow past an obstacle is interesting from a practical view point, because we can see such flows often in daily life related with a butterfly valve, a pier of a bridge etc.. It is also interesting from a purely hydrodynamical view point because the flow, for example, can be taken as a process in which finite amplitude perturbations generated by the obstacle interact with the Poiseuille flow. As we will show in Section 5, a two-dimensional channel flow past an elliptic cylinder becomes unsteady even for a sub-critical Reynolds number of the Poiseuille flow with respect to small perturbations. It is also interesting to study processes by which vortices are born near the cylinder, brought away into the "main" Poiseuille flow, and then decay by the effect of viscosity.

Although many studies are already published on the evolution of vortices in a flow past an obstacle (See, for example, Ta Phuoc Loc 1980, Badr Dennis 1985 and references therein.), we find the study of Kawamura & Kuwahara (1984) to be the most interesting from the view point of numerical hydrodynamics:

(1) They proposed a new upwind difference scheme which can be applied with sufficient accuracy and stability to flows of $R = 10^5$.

(2) Using their new scheme, they clarify that a turbulent flow can be taken as a laminar unsteady flow which can be studied by a numerical solution of the Navier-Stokes equations without any special assumption. The agreement between their results and experiments is good for flows past a circular cylinder with a surface roughness for $R = 10^3 \sim 10^5$.

(3) They show a typical example of the use of Thompson et al's (1976) boundary-fitted curvilinear coordinate systems.

Based on the above prominent results, we expect that we can clarify aspects of channel flows past an obstacle if we proceed along the line of their method of solution.

In this paper, we study two-dimensional flows of viscous incompressible fluid past an elliptic cylinder in a rectilinear channel. Because we take this configuration as a cross section of a butterfly valve by a plane perpendicular to the rotation axis of the valve, the major axis of the cylinder that is selected has the same length as the channel width, and the center of the cylinder is placed on the midplane of the channel. Reynolds number R of the flow (with respect to half-width of the channel and mean velocity at the infinity upstream) and the angle of attack θ of the cylinder ranges, respectively, between 50 and 1000 and between $0°$ and $40°$. The thickness ratio of the cylinder is kept equal to 0.2.

As we stated above, we apply the new upwind difference scheme by Kawamura & Kuwahara (1984) to the stream function-vorticity formalism of the Navier-Stokes equations. We apply Thompson et al's (1976) boundary-fitted curvilinear coordinate system to transform a physical plane onto a simple calculation plane. The Poisson type equation of the stream function is solved by the line-Jacobi method. We use the idea by Shida et al (1983) to estimate the stream function on the cylinder. We apply the Euler explicit method to solve the vorticity equations.

We locate the boundary between the steady and unsteady flows in the R-θ plane. We clarify processes by which vortices are born near the cylinder, brought away into the "main" Poiseuille flow, and then decay by the effect of viscosity. We show the validity of Imai's (1958) drag formula in our problem. As a practical application, we compare our results with Kimura et al's (1980) experiments with respect to the pressure drop due to the valve, and to the torque-coefficient.

Sections 2, 3, 4 and 5 give, respectively, the formulations of the problem, numerical procedures, calculation procedures of flow parameters and results and discussion. Finally, Section 6 gives a summary of the results.

2. Formulation of the problem

2.1 Boundary fitted curvilinear coordinate system

Let us suppose an elliptic cylinder placed in a rectilinear channel. The major axis of the cylinder has the same length as the channel width, and the center of the cylinder is placed on the midplane of the channel. The thickness ratio of the cylinder is kept equal to 0.2, and θ ranges between $0°$ and $40°$. The up- and the down-stream boundaries of the channel are located, respectively, at $x=-x_0$ and x_0, where we use the Cartesian coordinate system, as is shown in Figure 1. The coordinates are non-dimensionalised with respect to the half-width L_0 of the channel. The value of x_0 is kept equal to 20 in our computations.

Following the idea of the boundary-fitted curvilinear coordinate system proposed by Thompson et al (1976), we transform the physical plane onto a rectangular calculation plane. We use an 'O-type' transformation, as is shown in Figure 2. The mapping functions;

$$x=x(\xi, \eta), \qquad (2-1)$$

$$y=y(\xi, \eta), \qquad (2-2)$$

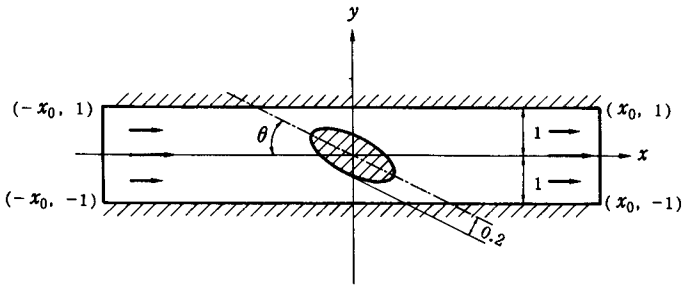

Figure 1. Geometrical configuration of our flow. Because we take this configuration as a cross section of a butterfly valve by a plane perpendicular to its rotation axis, the major axis of the elliptic cylinder has the same length as the channel width, and the center of the cylinder is placed on the midplane of the channel.

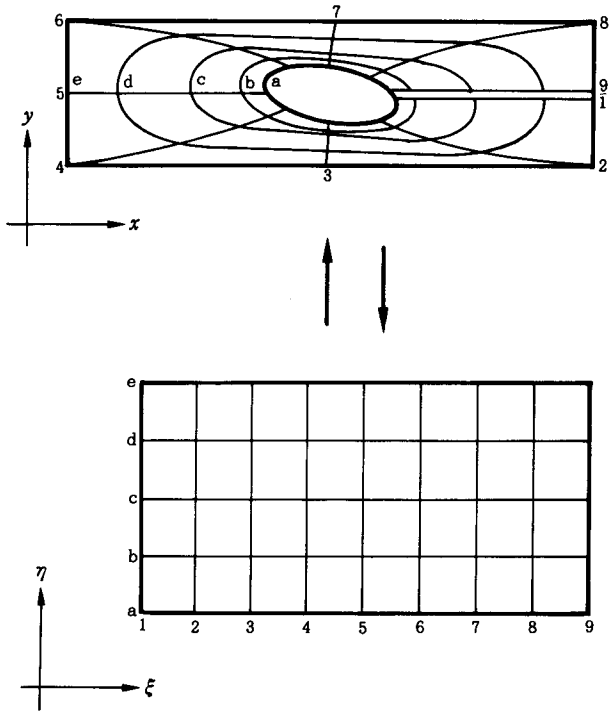

Figure 2. Correspondence between physical and calculation planes. The corresponding lines are referred to by the same notations.

satisfy the Poisson type equations on the calculation plane:

$$\alpha x_{\xi\xi} - 2\beta x_{\xi\eta} + \gamma x_{\eta\eta} = -J^2 \{x_\xi P(\xi, \eta) + x_\eta Q(\xi, \eta)\}, \quad (2-3)$$

$$\alpha y_{\xi\xi} - 2\beta y_{\xi\eta} + \gamma y_{\eta\eta} = -J^2 \{y_\xi P(\xi, \eta) + y_\eta Q(\xi, \eta)\}, \quad (2-4)$$

where (x, y) and (ξ, η) are, respectively, the Cartesian and curvilinear coordinate systems, P and Q are the sums of the exponential functions which include arbitrary parameters by which we can concentrate coordinate lines towards any point or curve in the physical plane, and

$$\alpha = x_\eta^2 + y_\eta^2, \quad (2-5)$$

$$\beta = x_\xi x_\eta + y_\xi y_\eta, \quad (2-6)$$

$$\gamma = x_\xi^2 + y_\xi^2, \quad (2-7)$$

$$J = x_\xi y_\eta - x_\eta y_\xi. \quad (2-8)$$

These are the quasi-linear elliptic systems of equations for $x(\xi, \eta)$ and $y(\xi, \eta)$ in the calculation plane. The boundary conditions are specified, based on the correspondence between the boundary points on the physical plane and those on the calculation plane. The solutions of (2 − 3) and (2 − 4), subject to these boundary conditions for an appropriate selection of P and Q, are obtained by the use of the TOMCAT code. (Thompson et al, 1977)

Figure 3 shows an example of the 81×65 coordinate lines generated for a case with $\theta = 17.5°$.

2. 2 Basic equation

A non-dimensional form of the stream function-vorticity formulation of the Navier-Stokes equations for a two-dimensional flow of viscous incompressible fluid is given as follows:

$$\omega_t + \Psi_y \omega_x - \Psi_x \omega_y = (\omega_{xx} + \omega_{yy})/R, \quad (2-9)$$

$$\Psi_{xx} + \Psi_{yy} = -\omega, \quad (2-10)$$

where Ψ is the stream function, ω the vorticity and R the Reynolds number with

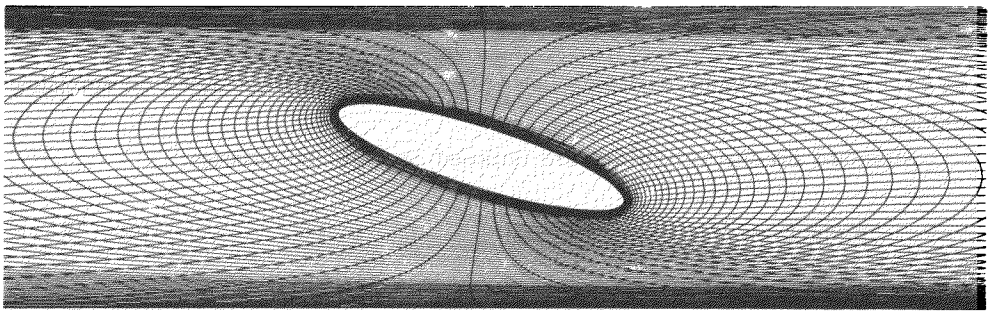

Figure 3. An example of the boundary fitted curvilinear coordinate system for the case with $\theta = 17.5^{\circ}$. The coordinate lines are concentrated toward the cylinder and toward the channel walls. This concentration is introduced to cope with rapid variations in flow properties near these boundaries.

respect to the mean velocity U_0 on the upstream boundary and the half-width L_0 of the channel.

By the use of ξ and η, (2 − 9) and (2 − 10) are transformed as follows:

$$\omega_t + (\Psi_\eta \omega_\xi - \Psi_\xi \omega_\eta)/J = \Delta\omega/R, \qquad (2-11)$$

$$\Delta\Psi = -\omega, \qquad (2-12)$$

where

$$\Delta A = (\alpha A_{\xi\xi} - 2\beta A_{\xi\eta} + \gamma A_{\eta\eta})/J^2 + PA_\xi + QA_\eta. \qquad (2-13)$$

2. 3 Boundary conditions

At the upstream boundary, the stream function and the vorticity are prescribed corresponding to a Poiseuille flow;

$$\Psi = 1.5 \cdot (y - y^3/3), \qquad (2-14)$$

$$\omega = 3y, \qquad (2-15)$$

at $x = -x_0$. At the downstream boundary, the boundary conditions are as follows;

$$\Psi_{xx} = 0, \qquad (2-16)$$

$$\omega_x = 0, \qquad (2-17)$$

at $x = +x_0$ in accordance with Roache's (1972) recommendation based on empirical evidences.

Standard no-slip conditions are imposed on rigid boundaries:

$$\Psi = \pm 1, \qquad (2-18)$$

$$\Psi_n = 0, \qquad (2-19)$$

at $y = \pm 1$ and

$$\Psi = \Psi_s, \qquad (2-20)$$

$$\Psi_n = 0, \qquad (2-21)$$

on the cylinder where plus and minus signs correspond respectively to the upper and lower walls, and the subscript n denotes the normal derivative on the rigid boundaries.

The value of Ψ_s is determined by the fact that the pressure is single-valued in the flow field. For a steady symmetric flow corresponding to the case of $\theta = 0°$, Ψ_s can be set equal to 0 in advance, because the flow is symmetric with respect to the midplane of the channel. As will be shown, however, the flow becomes unsteady and asymmetrical for a large Reynolds number, even in the case of $\theta = 0°$, As a matter of course, we can not expect any kind of flow symmetry for a case with the angle of attack. In such cases, specification of Ψ_s in advance is impossible, and Ψ_s is to be determined in the course of the calculation. We use Shida et al's idea (1983) to determine Ψ_s. Because (2 − 12) is linear with respect to Ψ, we can decompose it into two parts:

$$\Psi = \Psi_1 + \lambda \Psi_0. \qquad (2-22)$$

The first part Ψ_1 is a solution of (2 − 12) subject to the boundary conditions (2 − 14), (2 − 16), (2 − 18) and (2 − 20) in which Ψ_s is an arbitrarily selected constant Ψ_{s0}. The second part Ψ_0 is a solution of the Laplace equation subject to the boundary conditions:

$$\Psi_0 = 1 \qquad \textit{on the cylinder surface,} \qquad (2-23)$$

$\Psi_0 = 0$ *on the other boundaries.* (2 − 24)

Parameter λ is determined by the requirement that Ψ gives a single-valued pressure in the flow field. This condition is expressed by

$$\oint_c dp = 0, \tag{2-25}$$

where c is an arbitrarily closed path around the cylinder. Once λ is thus determined, the value of Ψ_s can be given as $\Psi_s = \Psi_{s0} + \lambda$.

3. Numerical procedures

In order to solve numerically (2 − 11) and (2 − 12) subject to (2 − 14) − (2 − 21), we use the finite difference approximations of the above equations. The values of $\Psi(\xi, \eta, t)$ and $\omega(\xi, \eta, t)$ at $(\xi_i, \eta_j, t) = (i\Delta\xi, j\Delta\eta, k\Delta t)$ are referred to as $\Psi^k_{i,j}$ and $\omega^k_{i,j}$, respectively. Here, $\Delta\xi$, $\Delta\eta$ and Δt are mesh spacings in the calculation plane and time step in our computations. The integers (i, j) and k refer to a mesh point and a certain instant of time. The superscript k is omitted hereafter for the sake of simplicity.

The time integration of (2 − 11) is carried out by the Euler explicit method. Second order central difference schemes are used for spacial derivatives in duffusion terms. The third order upwind difference scheme proposed by Kawamura & Kuwahara (1984) is used for the convection terms. These selections of schemes enable us to integrate (2 − 11) robustly with sufficient accuracy for high Reynolds number flows. The size of the time step is equal to the viscous diffusion time multiplied by a factor of the order of 10^{-1}. The criterion by which our solution is taken to have converged to a steady limit is that a steadiness parameter r becomes less than a certain tolerance. The parameter r is a ratio of the absolute value of the time derivative to the absolute sum of the space derivatives;

$$\begin{aligned} r = |\omega_t| / \{ & |\Psi_\eta \omega_\xi / J| + |\Psi_\xi \omega_\eta / J| \\ & + (|\alpha\omega_{\xi\xi}| + |2\beta\omega_{\xi\eta}| + |\gamma\omega_{\xi\xi}|)/(J^2 R) \\ & + (|P\omega_\xi| + |Q\omega_\eta|)/R \}. \end{aligned} \tag{3-1}$$

The above criterion is given as follows;

$$r<\varepsilon', \tag{3-2}$$

where ε' is a small parameter ($\sim 10^{-2}$). To avoid an unnecessarily strict application of the criterion, this criterion is applied to the flow region for which the following inequality is satisfied;

$$|\omega| > \delta' |\omega|_{max}, \tag{3-3}$$

where $|\omega|_{max}$ is the maximum absolute value of ω, and δ' is a small number ($\sim 10^{-4}$).

Equation (2 − 12) is solved by the line-Jacobi method of iteration. Second order central difference schemes are used for space derivatives, unless otherwise noted. The criterion of the convergence of the iteration is that a summation of the absolute relative increments of the stream function with respect to iteration over whole grid points is less than the product of a certain tolerance ε and the number of grid points N;

$$\sum_{i,j} |\Psi_{ij}^{n+1} - \Psi_{ij}^{n}| / (|\Psi_{ij}^{n+1}| + \delta) < \varepsilon N, \tag{3-4}$$

where n refers to the iteration step, and δ is a small positive number added to the denomitator in order to avoid zero dividing difficulties. In our computations, ε and δ are set equal to 10^{-4} and 10^{-3}, respectively.

The condition (2 − 16) on the downstream boundary reduces (2 − 10) to an ordinary differential equation for Ψ with respect to y. This equation is solved by the use of the central difference sheme and the Thomas implicit algorithm. By the use of this Ψ, the outflow boundary condition for Ψ becomes a Dirichlet type. The arbitrary constant Ψ_{s0} mentioned in the last section is set equal to the value of Ψ_s at the final stage of a computation which is finished just previous to the computation at hand. We take the cylinder surface as the path of integration in (2 − 25);

$$\oint_c dp = \int_{\xi_{min}}^{\xi_{max}} p_\xi \, d\xi = \int_{\xi_{min}}^{\xi_{max}} \{(\beta\omega_\xi - \gamma\omega_\eta)/J\} \, d\xi = 0, \tag{3-5}$$

where the line integration is performed by the trapezoidal rule, and ω_ξ and ω_η are evaluated from $\Psi = \Psi_1 + \lambda\Psi_0$. Because (3 − 5) depends linearly on λ, this is readily solved with respect to λ.

The vorticity on rigid boundaries is determined by the no-slip conditions (2 − 19) and (2 − 21). Taking into account that Ψ is constant along a rigid

boundary, we can reduce (2 − 10) and (2 − 19) or (2 − 21), respectively, as follows;

$$\omega = -\gamma \Psi_{mm}/J^2, \tag{3-6}$$

$$\gamma^{1/2}\Psi_{\eta}/J = 0. \tag{3-7}$$

The second order difference formula for (3 − 6), which implicitly satisfies (3 − 7), is used to evaluate ω on the rigid boundary. A special formula for Ψ_{η} is required at a point adjacent to the rigid boundary so as to avoid any inconsistency of accuracy of the difference schemes relevant to (3 − 6) and (3 − 7) (Briley 1971). The formulae on the cylinder surface, for example, are;

$$\Psi_{mm}|_{i,1} = (-7\Psi_{i,1} + 8\Psi_{i,2} - \Psi_{i,3})/(2(\Delta\eta)^2), \tag{3-8}$$

$$\Psi_{\eta}|_{i,2} = (-5\Psi_{i,1} + 4\Psi_{i,2} + \Psi_{i,3})/(4\Delta\eta), \tag{3-9}$$

where i refers to a point on the cylinder along which $j = 1$.

4. Flow parameters

Once the velocity distribution is determined, the pressure is obtained by line integrations based on the primitive form of the Navier–Stokes equations. We start the integration from the upstream boundary and set the starting value of the pressure equal to zero. In practice, we perform the integration either along an upper channel wall, or along an approximate stagnation stream line which consists of lines of the constant ξ and a line of the constant η.

The integrals along a line of η=constant and and ξ=constant are, respectively, as follows:

$$p(\xi_0) - p(\xi) = -R[u^2/2]_{\xi}^{\xi_0} + \int_{\xi}^{\xi_0} [-R\omega\Psi_{\xi} + \{\beta(R\Psi_{\xi\eta} + \omega_{\xi}) - \gamma(R\Psi_{\eta\eta} + \omega_{\eta})\}/J]\, d\xi, \tag{4-1}$$

$$p(\eta_0) - p(\eta) = -R[u^2/2]_{\eta}^{\eta_0} + \int_{\eta}^{\eta_0} [-R\omega\Psi_{\eta} + \{\alpha(R\Psi_{\xi\eta} + \omega_{\xi}) - \beta(R\Psi_{\eta\eta} + \omega_{\eta})\}/J]\, d\xi. \tag{4-2}$$

Forces on the cylinder surface are given as

$$X = (-p + 2u_x)(-y_\xi) + (u_y + v_x)x_\xi, \tag{4-3}$$

$$Y = (u_y + v_x)(-y_\xi) + (-p + 2v_y)x_\xi, \tag{4-4}$$

where X and Y are the $x-$ and $y-$components of the force, respectively, and use is made of the fact that η is constant on the surface.

Combining the continuity equation and no-slip conditions on the cylinder, we obtain;

$$-v_y x_\xi + u_y y_\xi = 0, \tag{4-5}$$

$$v_x x_\xi - u_x y_\xi = 0. \tag{4-6}$$

Using the above, we can modify X and Y as follows:

$$X = py_\xi - \omega x_\xi, \tag{4-7}$$

$$Y = -px_\xi - \omega y_\xi. \tag{4-8}$$

The drag-coefficient C_D and the lift-coefficient C_L are obtained by the respective integrations of X and Y along the cylinder surface;

$$C_D = (1/R)\int_{\xi_{min}}^{\xi_{max}} (py_\xi - \omega x_\xi)\, d\xi, \tag{4-9}$$

$$C_L = (1/R)\int_{\xi_{min}}^{\xi_{max}} (-px_\xi - \omega y_\xi)\, d\xi, \tag{4-10}$$

where ξ_{min} and ξ_{max} refer, respectively, to the minimum and the maximum values of ξ, and the factor $(1/R)$ is multiplied because of our non-dimensionalization.

Moment coefficient is obtained by the following:

$$C_M = (1/R)\int_{\xi_{min}}^{\xi_{max}} \{(py_\xi - \omega x_\xi)y + (px_\xi + \omega y_\xi)x\}\, d\xi. \tag{4-11}$$

For the sake of comparison with experiments, we define the pressure drop due to the cylinder and the torque coefficient of the cylinder. The pressure drop due to the cylinder Δp_{valve} is the difference between our pressure drop Δp and the pressure drop $\Delta p_{Poiseuille}$ of a simple Poiseuille flow. Here, the pressure drop is defined as the pressure difference between the up- and downstream boundaries;

$$\Delta p_{valve}=\Delta p-\Delta p_{Poiseuille}, \qquad (4-12)$$

$$\Delta p_{Poiseuille}=3\cdot 2x_0. \qquad (4-13)$$

The torque coefficient is a ratio of the moment coefficient to the pressure drop due to the valve;

$$C_T=(R/8)\cdot(C_M/\Delta p), \qquad (4-14)$$

where the factor $(R/8)$ is multiplied, for the same reasoning as above.

5. Results and discussion

The computations were performed on Fujitsu VP-200, M-382 at the Data Processing Center of Kyoto University. For cases of steady limiting flow, computations are continued for several tens of thousand time steps until the steadiness criterion $(3-2)$ is fulfilled. For cases of unsteady limiting flow, periodicity of the limiting flow is examined based on the time variations of the lift-, drag- and moment-coefficient as are shown in Figures 8 and 12. The computations are continued for several tens through hundred thousand time steps until we have confidence on the periodicity of the limiting flows.

Before the discussion of our results, we examine first the accuracy of our numerical results:

(1) To examine errors caused by the finite location of the up- and downstream boundaries, we compare two cases of $x_0=20$ and 30 for the flow with $R=500$ and $\theta=0°$. Both flow patterns show good agreement with each other. The relative differences in the drag coefficient and the pressure drop due to the cylinder are, respectively, 0.8% and 3.4%.

(2) To examine errors caused by the mesh spacing, we recalculate a flow with $R=1000$ and $\theta=0°$ by the use of twice as many grid points with respect to η. The recalculated flow pattern is in good agreement with that of the original mesh spacing. The relative difference in the drag coefficient is 4.7%. A similar recalculation is made for a flow with $R=300$ and $\theta=25°$ by the use of twice as many grid points with respect to ξ. Again, the recalculated flow pattern is in good agreement with that of the original mesh spacing. The relative differences in the drag coefficient and the pressure drop due to the cylinder are, respectively, 1.8% and 4.2%.

(3) To examine the effect of the initial conditions for the final periodic states of the flows which tend to an unsteady solution, we compare two flows with

$R=200$ and $\theta=15°$. The initial conditions are equal to the final states of flows with the same θ and $R=300$ and 100, respectively. The agreement of the results for these two cases is excellent. It assures us that the final periodic state of the unsteady flow is not affected by our selection of the initial conditions.

Pairs of Reynolds number and angle of attack for which we have performed numerical calculations are given in Figure 4. We also include information as to whether the flow corresponding to a pair is steady or unsteady. The threshold Reynolds number at which the flow becomes unsteady is estimated as $400 \sim 500$ for $\theta=0°$. This is rather large in comparison with an approximate value of 50 for a flow past a circular cylinder. (See, for example, Batchelor 1967.) The length scale of wavy motion of wake for a fully unsteady case of $R=1000$ (Figure 7) is nearly equal to the chord length of the cylinder, and the motion damps out within about two wave lengths towards downstream. These aspects are in good contrast to those of a flow of $R=55$ past a circular cylinder in which the wave

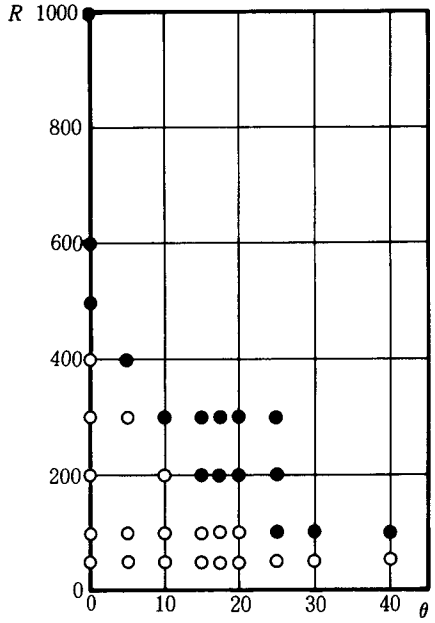

Figure 4. Pairs of Reynolds number and the angle of attack for which computations are performed. The open and filled circles indicate that the corresponding flows tend to steady and unsteady limiting states, respectively. This figure is to be taken as defining a boundary between the steady and unsteady flows in the $R-\theta$ plane.

length is several times as long as the diameter, and the wavy motion lasts for several wave lengths (Batchelor 1967). The stabilizing effect of the Poiseuille flow may be the most important cause of the above differences. The decrease of this threshold Reynolds number with the increase of the angle of attack seems to make a "phase transition" at $\theta = 25°$. Up to this angle of attack, we can clearly define the inclination of the decrease with respect to θ. For larger angles of attack, on the contrary, the threshold value seems to be levelled out to stay between 50 and 100. For the former angles of attack, we can understand the flow as a unified entirety of the Poiseuille flow past a cylinder. For the latter angles of attack, however, the flow is better understood as being interaction processes of two jets which emerge, respectively, from the upper and the lower sub-channels between the cylinder and channel walls. We can recognize this fact in flow configurations in Figure 9 (b) and (d).

The change of the flow configuration with the Reynolds number for the case of $\theta = 0°$ is given in Figures 5 and 6. We can see the change in which a counter current region near the trailing edge is elongated towards the downstream direction to show a wavy appearance at $R = 500$. An example of the time development of unsteady flows is given in Figure 7, in which flow configurations near the stagnation stream line are given for a time span corresponding to one cycle of the periodic changes of the flow parameters in Figure 8. We can see how a vortex is born either on the upper or the lower side near the trailing edge, grows up and is brought into the region of the "running current" to be damped out finally by the effect of viscosity.

The changes of the flow configurations with an angle of attack for the case of $R = 100$ are given in Figures 9 and 10. We can recognize clearly the above mentioned "phase transition" in which the Poiseuille flow past a cylinder effectively changes to two interacting jets. These jets emerge respectively from the upper and the lower sub-channels between the cylinder and original channel. Also interesting is the appearance of fairly large regions of counter currents both on tne upper and the lower channel walls downstream of the cylinder for the case of $\theta = 40°$. Figure 11 gives the time development of the flow pattern for the case with $R = 300$ and $\theta = 25°$. We can clearly see periodic time evolutions of vortices which are strongly asymmetric with respect to the midplane of the channel. The asymmetry manifests itself also in the time changes of the flow parameters in Figure 12.

Figure 13 gives the drag coefficient C_D versus R for cases with $\theta = 0°$. The filled circles give our results, and the solid line corresponds to Imai's formula (1958) of a drag coefficient:

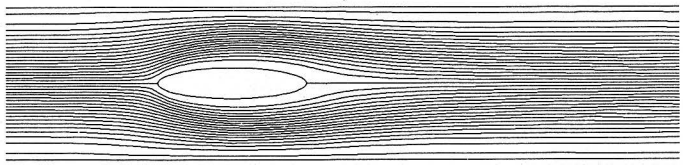

(a) $R=50.$

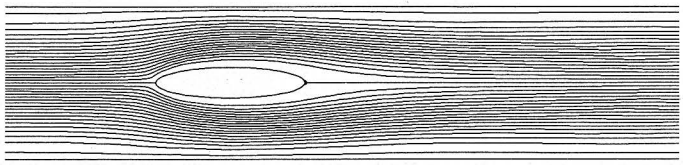

(b) $R=100.$

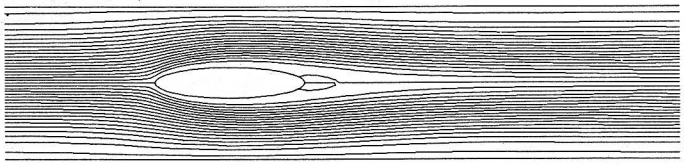

(c) $R=300.$

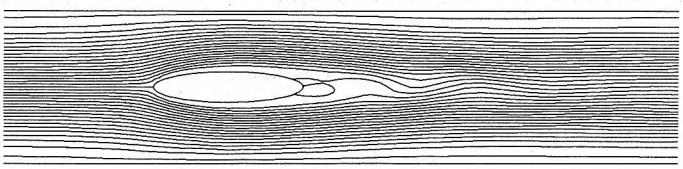

(d) $R=500.$

Figure 5. Stream lines at the final stages of computations for cases with $\theta=0°$. The small unnatural behaviors of stagnation stream lines for $R=300$ and 500 are caused by our graphics subroutine, and are not to be taken seriously. We can see how a counter current region near the rear stagnation point is elongated toward the downstream direction with the increase of R. We can see also that the flow for $R=500$ is unsteady, based on the wavy configuration of stream lines.

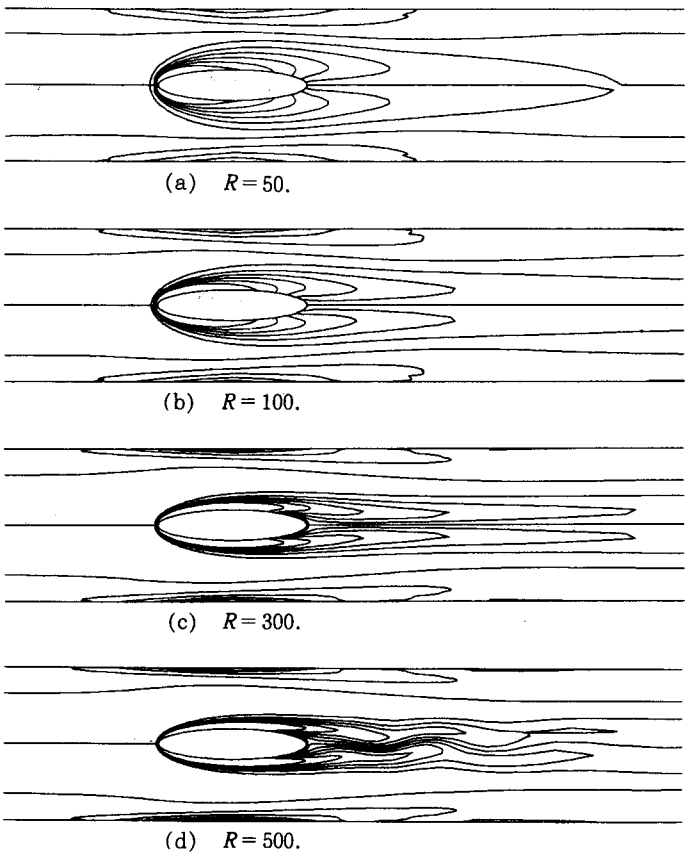

Figure 6. Equi-vorticity lines at the final stages of computations for cases of $\theta=0°$. We can see a correspondence between the vorticity configurations in this figure and those of the stream lines in Figure 5.

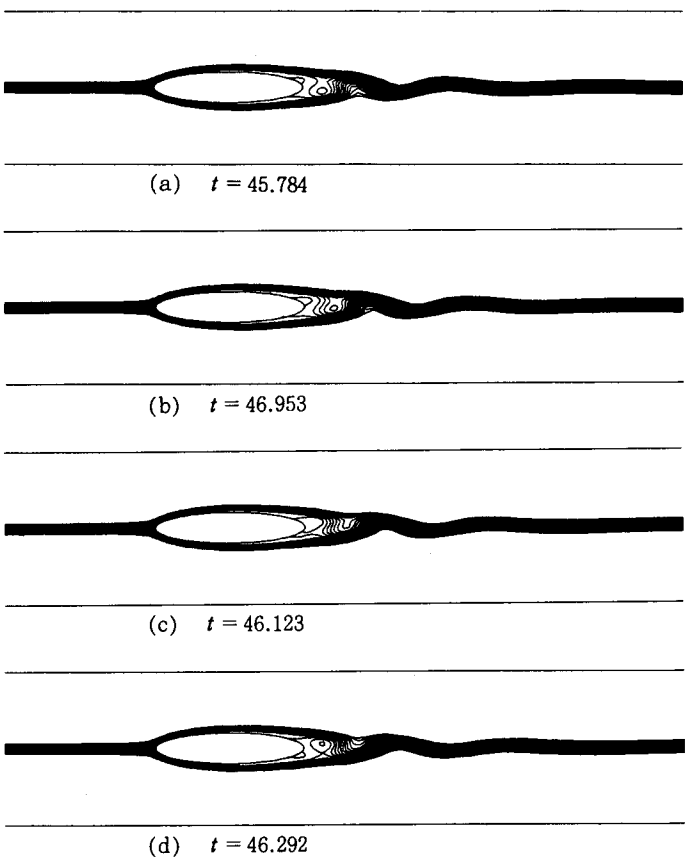

Figure 7. Time development of stream line configuration for a case with $R = 1000$ and $\theta = 0°$. The time durations from (a) to (h) correspond to one cycle of periodic time changes of

(e) $t = 46.462$

(f) $t = 46.631$

(g) $t = 46.801$

(h) $t = 46.971$

flow parameters in Figure 8. We can see how vortices are born near the cylinder, brought away into "main" Poiseuille flow, and then decay by the effect of viscosity.

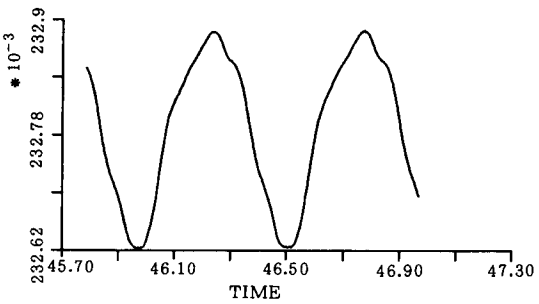

(a) C_D

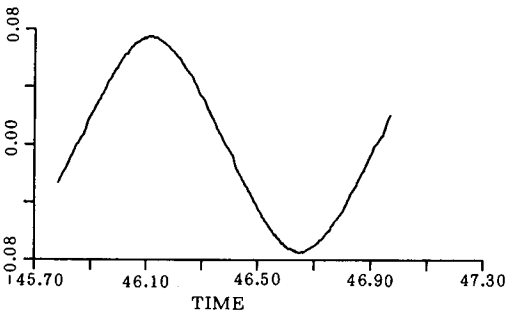

(b) C_L

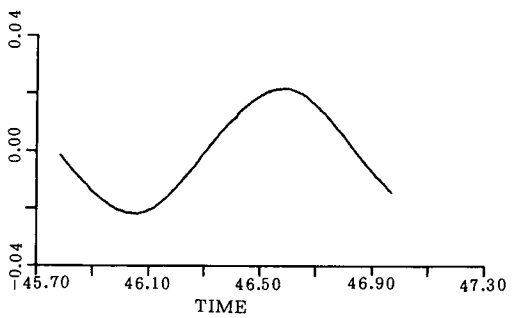

(c) C_M

Figure 8. Periodic time changes of flow parameters for a case with $R = 1000$ and $\theta = 0°$.

$$C_D^{1/2} = 0.279 + 6.56 \cdot R^{-1/2}, \qquad (5-1)$$

where the first term and the factor of the second term on the right hand side are estimated by our results for $R = 100$ and 400. The dashed line corresponds to Stokes law of drag:

$$C_D = 71.5/R, \qquad (5-2)$$

where the factor on the right hand side is estimated by our result for $R = 50$. The agreement of our results with Imai's formula is surprisingly good, if we take into account that the formula is derived for the case of an unbounded flow around an obstacle. We suppose that the formula has an unexpectedly wide applicability.

Figure 14 gives the polar diagram of a drag coefficient versus a lift coefficient. The filled rhombuses, circles, triangles and rectangles give our results for $R = 50$, 100, 200 and 300, respectively. The dash-dotted, solid, dashed and dotted lines are produced based on the simple formula:

$$C_D = C_{D0} + kC_L^2, \qquad (5-3)$$

where the factors k are estimated to be 0.081, 0.116, 0.162 and 0.179, respectively, for $R = 50$, 100, 200 and 300. It is an interesting coincidence that our results can be summarized by the same type of formula as that of lifting aerofoil, despite the fact that almost all of our flow configurations belong to those of stalled aerofoils.

As a practical application, we compare our results with the experiments by Kimura et al (1980) of a flow past a butterfly valve in a rectilinear circular pipe. Although the above two flows seem to be completely different at first glance, we believe that the above comparison does make sense. The reasons for our belief are as follows:

(1) The geometrical configuration of a cross section of the valve by an arbitrary plane perpendicular to the valve axis is the same as that of our problem.

(2) Because of the above situation, we can roughly estimate a flow parameter slicing the flow field by planes perpendicular to the valve axis. We estimate the parameter for the sliced flow based on the two-dimensional flow with same geometrical configuration, and finally integrate the estimates over the whole valve.

Because flow parameters like drag-, lift- and moment-coefficient of unsteady flows oscillate periodically with respect to time, we use these time averages for

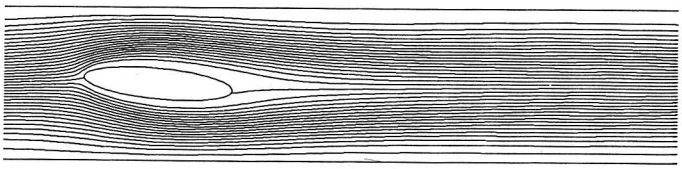

(a) $\theta = 5.0$

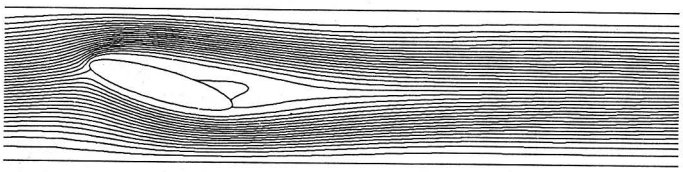

(b) $\theta = 15.0$

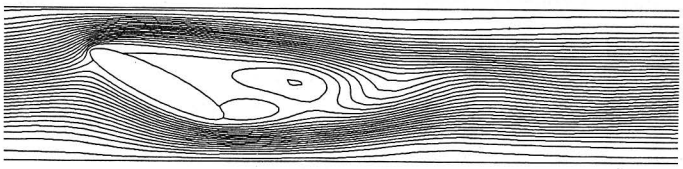

(c) $\theta = 25.0$

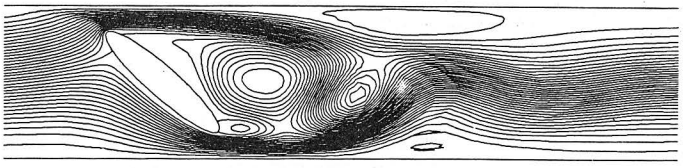

(d) $\theta = 40.0$

Figure 9. Stream lines at the final stages of computations for cases with $R = 100$ and various angles of attack. The wavy configurations for $\theta = 25°$ and $40°$ come from the fact that the corresponding flows are unsteady. The flow for $\theta = 40°$ can be taken as interaction processes of two jets which emanate, respectively, from the upper and lower sub-channels between the cylinder and original channel walls. It is also interesting that there appear considerably large stagnant regions near the channel walls downstrean of the cylinder.

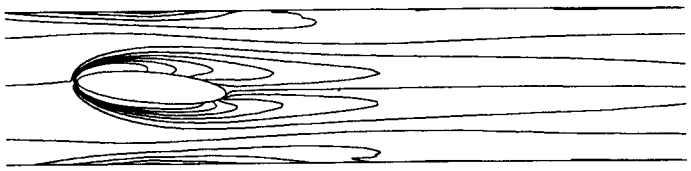

(a) $\theta = 5.0$

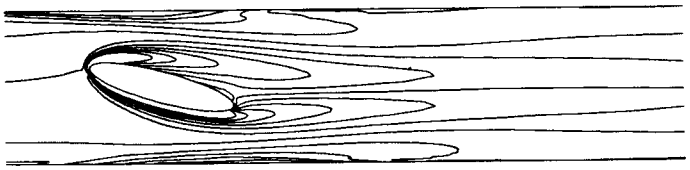

(b) $\theta = 15.0$

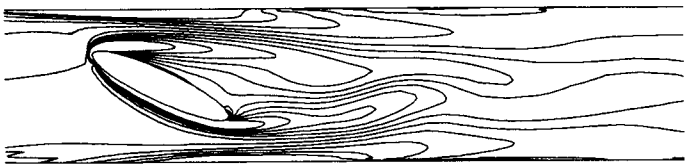

(c) $\theta = 25.0$

(d) $\theta = 40.0$

Figure 10. Equi-vorticity lines at the final stages of computations for cases with $R = 100$ and various angles of attack. We can see a correspondence between the vorticity configurations in this figure and those of the stream lines in Figure 9.

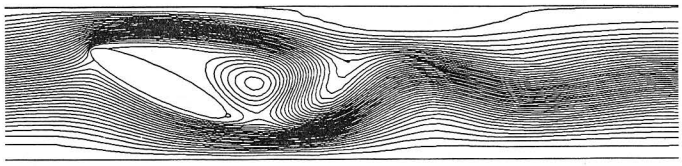

(a) $t = 31.160$

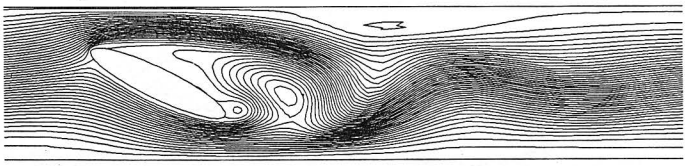

(b) $t = 31.585$

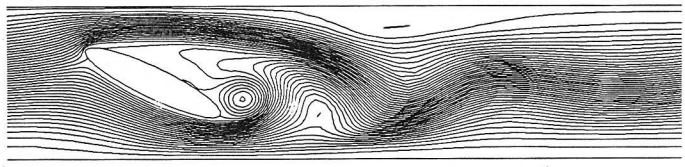

(c) $t = 32.010$

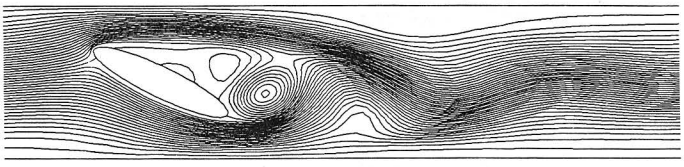

(d) $t = 32.435$

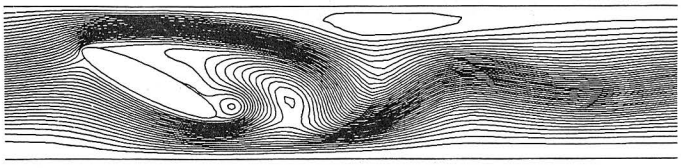

(e) $t = 32.860$

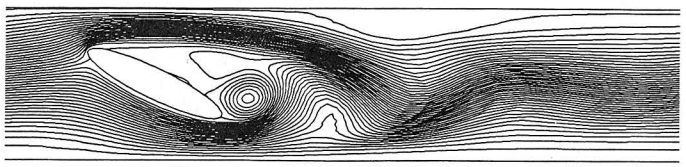

(f) $t = 33.285$

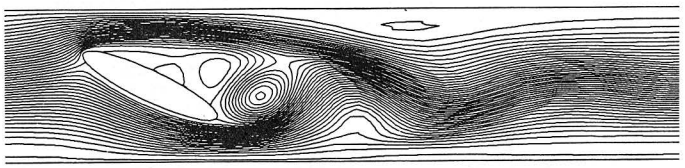

(g) $t = 33.710$

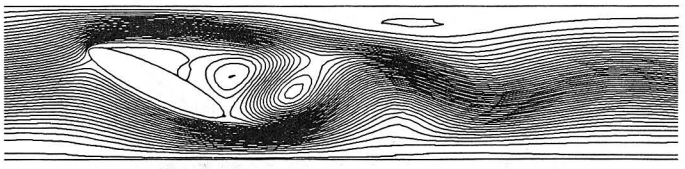

(h) $t = 34.135$

Figure 11. Time development of stream lines for a case with $R = 300$ and $\theta = 25°$. The time durations from (a) to (h) correspond to one cycle of periodic time changes of the flow parameters in Figure 12. We can see asymmetric vorticity motions with respect to the midplane of the channel in this case. The asymmetry manifests itself also in the time changes of the flow parameters in Figure 12.

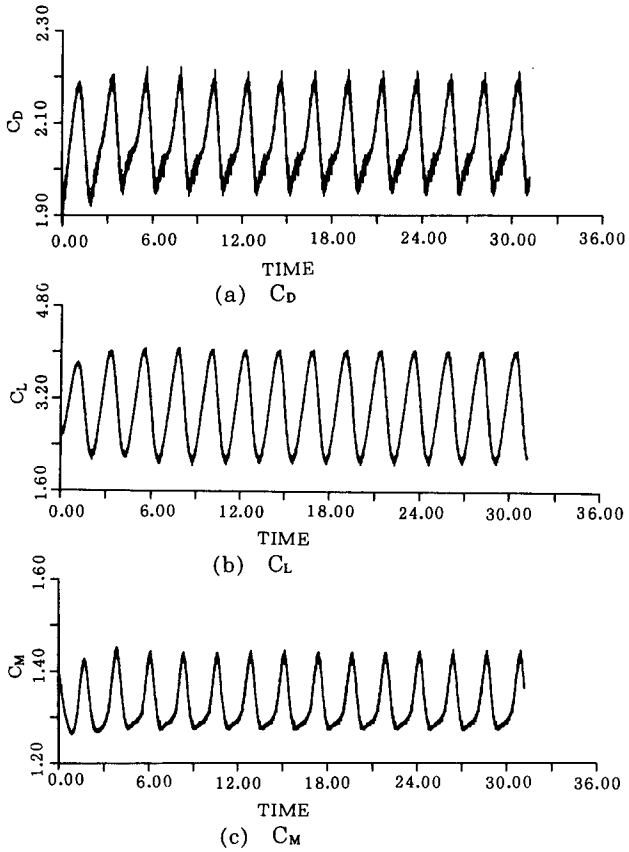

Figure 12. Periodic time changes of flow parameters for a case with $R=300$ and $\theta=25°$. This figure covers the whole time span, from the initial to the final stage of computation. The periodicity of the time changes is clear except for a transient phase of variation from the initial state, which is assumed to be equal to the final state for a case with $R=200$.

the above comparison. As a matter of fact, Kimura et al (1980) gave timely stationary results for the pressure drop due to the valve, and for the torque-coefficient. On the contrary, we can not use the time average of the pressure drop due to the cylinder, because the time consuming calculation of the pressure drop is performed only for the final stage of each computation. This causes a clumsy situation from the view point of the above comparison. A remedy for this situation will be given in the following.

Figure 15 gives the pressure drop due to the elliptic cylinder. This quantity gives us an estimate of the loss of the pressure head caused by the cylinder.

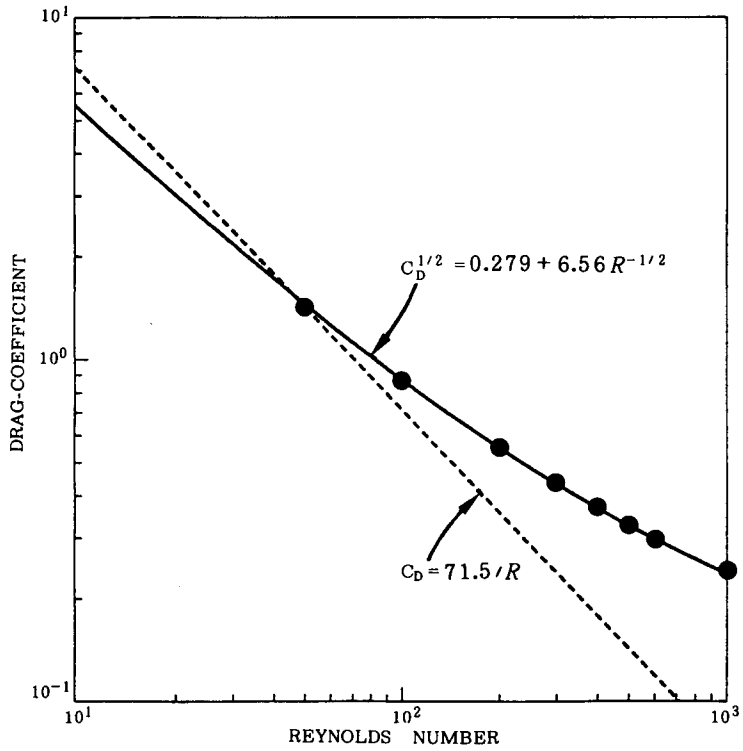

Figure 13. Drag coefficient diagram versus Reynolds number for cases with $\theta = 0°$. The filled circles give our results, and the solid line is given based on Imai's drag formula: $C_D^{1/2} = A + B \cdot R^{-1/2}$, the coefficients A and B of which are determined by our results for $R = 100$ and 400. The dotted line shows Stokes' law of drag: $C_D = A/R$, the coefficient A of which is determined by our result for $R = 50$. The agreement between our results and Imai's drag formula is surprisingly good, if we take into account that the formula is derived for an unbounded flow past an obstacle.

Because of our reasoning (2) above, we compare our results directly with Kimura et al's (1980) formula:

$$\Delta P_{valve} = \Delta P_{valve,1} + \Delta P_{valve,2}, \qquad (5-4)$$

$$\Delta P_{valve,1} = 2R[1/((1-\sin\theta)(2-s\theta^m)) - 0.5]^2, \qquad (5-5)$$

$$\Delta P_{valve,2} = (\Delta P_{valve})_0 \cos\theta, \qquad (5-6)$$

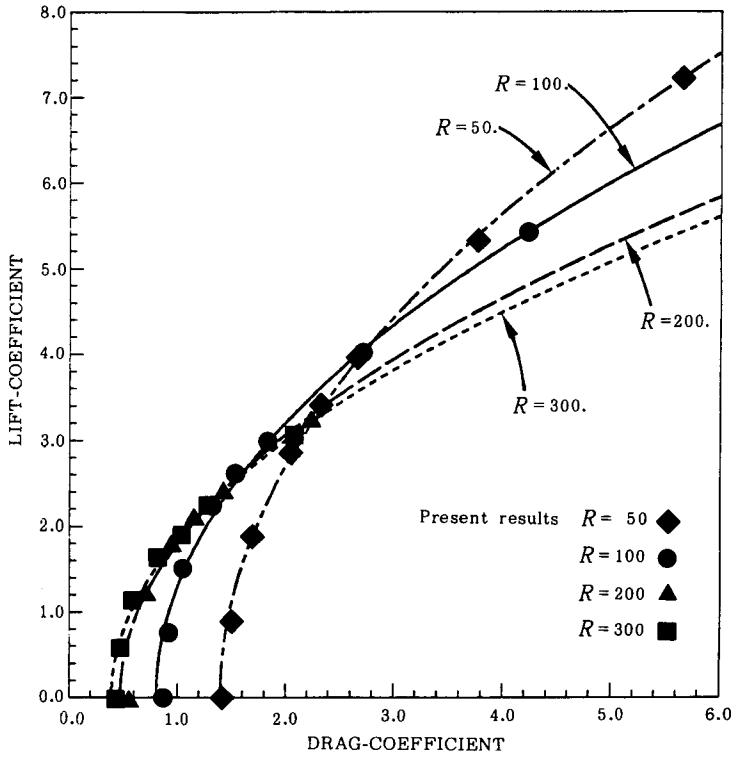

Figure 14. Polar diagram of drag-coefficient versus lift-coefficient. The dash-dotted, solid, dashed and dotted lines correspond, respectively, to cases with $R=50$, 100, 200 and 300. These are given based on the formula : $C_D = A + B \cdot C_L^2$, the coefficients A and B of which are determined by the least square fit to our results. It is an interesting coincidence that our results are summarised by the same type of relation between the drag- and lift-coefficient as that for the lifting aerofoil, despite the fact that our flow configuration belongs to that of the stalled aerofoil.

where $(\Delta P_{valve})_0$ is the pressure drop due to the valve for the case of $\theta = 0°$ and s and m are the free parameters. The formula is to be taken as a rule of thumb based on Kimura et al's (1980) experiments. For the sake of comparison, we estimate parameters s and m based on our results for $\theta = 10°$ and 25° for each group of cases with $R=50$, 100, 200 and 300. We give the respective resulting curves in Figure 15, in which notations are the same as those in Figure 14. The agreement between our results and the above formula is good, except that our result for $\theta = 40°$ and $R=100$ obviously deviate from the formula. As is given in

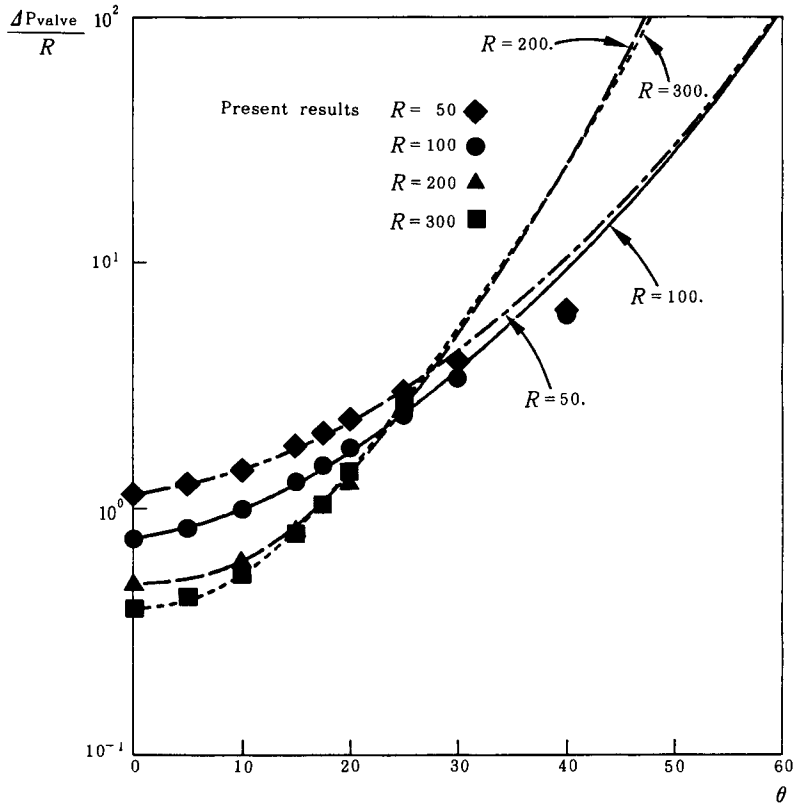

Figure 15. Pressure drop due to the cylinder versus angle of attack. The lines are given based on the empirical relations (5 − 4) − (5 − 6), the coefficients s and m of which are determined by our results for $\theta = 10°$ and 25°. Our results for cases with $R = 50$ and 100 and $\theta = 40°$ deviate considerably from the corresponding lines. The main cause of this deviation is ascribed to the situation in which our pressure drop is calculated only at the final stage, and is not its time average. We estimate the pressure drop, therefore, by these curves rather than by our results hereafter.

(4 − 1) and (4 − 2), the calculation of the pressure drop needs derivatives of vorticity. Thus, it is to be expected to include rather large errors in comparison with other quantities. Figure 16 gives the pressure distributions along the upper channel wall and along the approximate stagnation stream line for the above case. The inclination of the dashed straight line is the same as the pressure gradient of the "main" Poiseuille flow. The relative difference between the pressure drops along the above two lines is estimated to be 10%. This estimate gives us an idea about errors in a calculation based on (4 − 1) and (4 − 2).

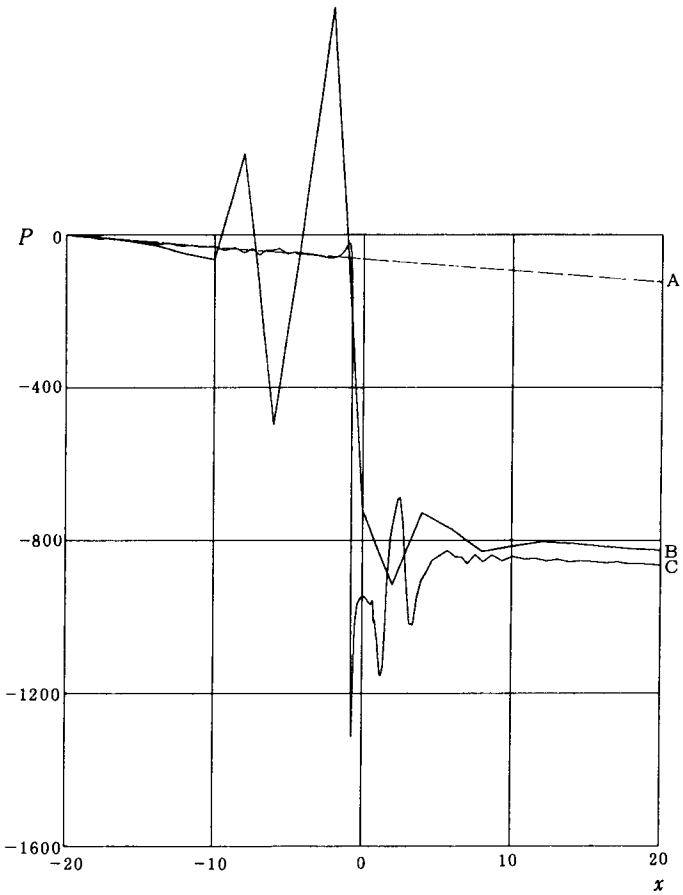

Figure 16. Pressure distributions along the upper channel wall and along the approximate stagnation stream line for a case with $R=100$ and $\theta=40°$. The pressure is estimated at the final stage of computation, and does not necessarily coincide with its time average. The dashed straight line has the same inclination as the pressure gradient of the "main" Poiseuille flow. The segments AB and AC on the right side of the figure give us the pressure drop due to the cylinder estimated, respectively, along the upper channel wall and along the approximate stagnation stream line. A relative difference of 10% between these estimates gives us a rough estimate of the accuracy of our pressure calculation based on (4 − 1) and (4 − 2).

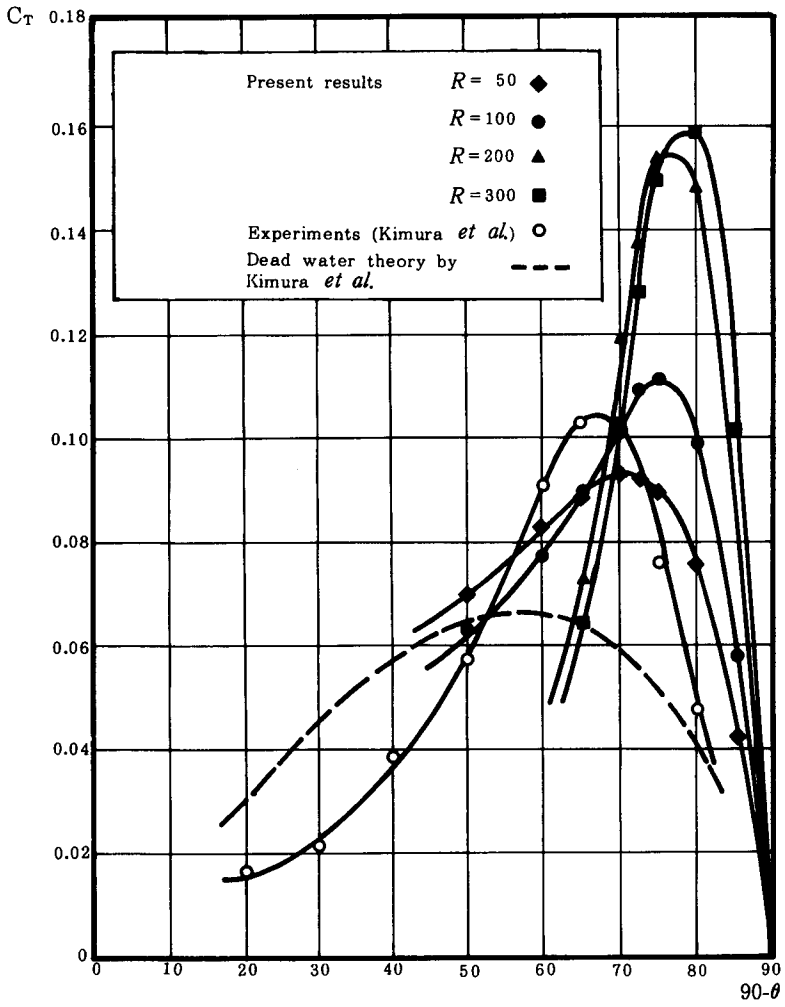

Figure 17. Torque-coefficient versus angle of attack. The open circles give Kimura et al's (1980) experiments, and the dashed line gives their theoretical estimates based on the dead water theory of a two-dimensional unbounded flow past a flat plate. In contrast to the results by the dead water theory, our results well reproduce a steep crest in the experiments. The best quantitative agreement between our results and experiments is obtained for cases with $R=50\sim100$. This coincides with the empirical fact that flow parameters of turbulent flows can be reprocuced by laminar flow models with the effective Reynolds number 50.

This estimate is much smaller than the above deviation of more than 50%. As is noted above, another error is caused by the fact that the pressure is calculated only at the final time step. Hence, the calculated pressure drop does not necessarily coincide with its time average. Because of this situation, we do not use our results for the pressure drop, but estimates based on the curves in Figure 15 in the calculation of the torque-coefficient.

Figure 17 gives the touque-coefficient estimate, based on the above estimate of the pressure drop due to the cylinder and time average of the moment-coefficient. Our results can again be compared directly with Kimura et al's (1980) experiments which are given in the figure. Their theoretical results, based on the dead water theory of a two-dimensional unbounded flow past a flat plate, are also given. The curves in the figure are drawn to clarify the general trends of the results. In good contrast to the dead water theory, the steep crest which is characteristic of experiments is qualitatively well reproduced by our results. It is also interesting that our results with $R=50\sim100$ give the best agreement with experiments from a quantitative view point. This fact coincides with the empirical evidence that flow parameters of turbulent flows can be simulated by laminar flow models with the effective Reynolds number $40\sim50$. (Imai 1958)

6. Summary of results

Our results on the two-dimensional flow of viscous incompressible fluid past a thin elliptic cylinder in a rectilinear channel are summarized as follows:

1) We clarify the boundary between the steady and unsteady flows in an $R-\theta$ plane. (See Figure 4.) The inclination of the boundary with respect to the angle of attack of the cylinder seems to make a "phase transition" corresponding to the change in flow configuations. We study also processes by which vortices are born near the cylinder, brought away into the "main" Poiseuille flow, and then decay by the effect of viscosity. (See Figures 7 and 11.)

2) We show, for cases of $\theta=0°$, that our results on the drag coefficient can be well reproduced by Imai's (1958) formula: $C_D=A+B\cdot R^{-0.5}$ within our range of Reynolds number. (See Figure 13.) We suppose that the formula has an unexpectedly wide validity.

3) As a practical application, we compare our results with those of Kimura et al's (1980) experiments on a butterfly valve. We give reasonings by which our comparison does make sense, and note that we use time averages of the flow parameters in the above comparison. Agreement between our results and

experiments is qualitatively good for the pressure drop due to the valve, and for the torque-coefficient. The most interesting fact is that our results well reproduce a steep crest in the torque-coefficient diagram, which is characteristic of the experiments. Also interesting is the fact that the best quantitative agreement for the torque-coefficient is obtained for Reynolds number 50 ~ 100.

The above results 3), especially, assure us that our results on two-dimensional flows can be used as effective working models of three-dimensional channel flows.

Acknowledgement

The authors thank Professor Takuya Matsuda and Doctor Izumi Hachisu for their discussions. Also, we extend our thanks to Professor Takeyoshi Kimura for his stimulating and informative discussions on butterfly valves.

References

Badr, H. M. and Dennis, S. C. R., 1985, Time-dependent viscous flow past an impulsively started rotating and translating circular cylinder, J. Fluid Mech. **158**, 447 - 488

Batchelor, G. K., 1967, An Introduction to Fluid Dynamics, Plate 2 Fig. 4.12.6 Streak lines in the wake behind a circular cylinder (From Homann 1936 a), Cambridge Univ. Press

Briley W. R., 1971, A numerical study of laminar separation bubbles using the Navier-Stokes equations, J. Fluid Mech. **47**, 713 - 736

Imai, I., 1958, Theory of drag by fluid, (in Japanese), Kagaku **28**, 110 - 115

Kawamura, K. and Kuwahara, K., 1984, Comprtation of high Reynolds number flow around a circular cylinder with surface roughness, AIAA-84 - 0340, AIAA 22 nd Aerospace Sciences Meeting

Kimura, T., Kuwahara, C. and Yoneda J., 1980, Study of a butterfly valve, Mass flow-, torque- and cavitation-characteristics, (in Japanese), KR-F 02, Faculty of Eng., Kobe Univ.

Roache, P. J., 1972, Computational Fluid Dynamics, III-C-7. Outflow Boundary, 154 - 161, Hermosa Publishers, Albuquerque, New Mexico

Shida Y., Kuwahara, K. and Takami, H. 1983, Numerical study of flow past two circular cylinders, Proc. Second Asian Congress Fluid Mech., 686 - 691, Science Press, Beijing

Ta Phuoc Loc, 1980, Numerical analysis of unsteady secondary vortices generated by an impulsively started circular cylinder, J. Fluid Mech. **100**, 111 - 128

Thames, F. C., Thompson, J. F., Mastin, C. W. and Walker, R. L., 1977, Numerical solutions for viscous and potential flow about arbitrary two-dimensional bodies using body fitted coordinate systems, J. Comput. Phys. **24**, 245 - 273

Thompson, J. F., Thames, F. C. and Mastin, C. W., 1976, Boundary-fitted curvilinear coordinate systems for solution of partial differential equations on fields containing any number of arbitrary two-dimensional bodies, NASA CR-2729

Thompson, J. F., Thames, F. C. and Mastin, C. W., 1977, TOMCAT-A code for numerical generation of boundary-fitted curvilinear coordinate systems on fields containing any number of arbitrary two-dimensional bodies, J. Comput. Phys. **24**, 274-302